Crossing of the Distillation Boundary in Homogeneous Azeotropic Distillation: Influence of Interphase Mass Transfer

P. A. M. Springer, B. Buttinger, R. Baur, and R. Krishna*

Department of Chemical Engineering, University of Amsterdam, Nieuwe Achtergracht 166, 1018 WV Amsterdam, The Netherlands

Residue curve maps can be used to predict composition trajectories for packed and trayed distillation columns, provided that vapor and liquid phases are in thermodynamic equilibrium and the column is operating at total reflux. In the case of ternary azeotropic distillations, distillation boundaries divide the composition space into two, or more, regions. It has been mentioned in the literature that distillation boundaries that are straight lines cannot be crossed during actual column operation. The major objective of this paper is to show that interphase mass transfer in ternary azeotropic distillation leads to differences in the component Murphree efficiencies and that such differences can allow even straight-line distillation boundaries to be crossed. Experiments were carried out in a bubble-cap distillation column operated at total reflux. The investigated homogeneous azeotropic system water (1)−ethanol (2)−acetone (3) has a binary minimum-boiling azeotrope for the water−ethanol mixture, which leads to a simple distillation boundary between the azeotrope and pure acetone. Even though the distillation boundary is nearly straight, our experiments clearly demonstrate boundary-crossing phenomena. To rationalize our experimental results, we develop a rigorous nonequilibrium (NEQ) stage model, incorporating the Maxwell−Stefan diffusion equations to describe transfer in either fluid phase. The developed NEQ model anticipates the boundary-crossing effects and is in excellent agreement with a series of experiments carried out in different composition regions. In sharp contrast, an equilibrium (EQ) stage model fails even at the qualitative level to model the experiments. It is concluded that for reliable design of azeotropic distillation columns we must take interphase mass-transfer effects into account in a rigorous manner.

Introduction

There is considerable industrial interest in the design and optimization of homogeneous and heterogeneous azeotropic distillation. This interest stems from the large number of industrial columns in operation and the potential of developing improved separation schemes to minimize energy consumption. Residue curve maps are commonly used in the development of separation flow schemes.[1−3] The residue curve map is usually divided into separate regions by simple distillation region boundaries that act as impassable barriers to the residue curves in each of the regions. The existence, location, and curvature of distillation boundaries are very important in the synthesis of distillation column sequences.[1−19]

Levy et al.[12] have put forward the following two "rules" in continuous azeotropic distillations:

(1) If the simple distillation boundary is perfectly linear, then the steady-state composition profile in a continuous distillation column cannot cross the boundary from either side.

(2) If the simple distillation boundary is curved, then the steady-state composition profile in a continuous distillation column cannot cross the boundary from the concave side but may cross the boundary from the convex side when moving from the product compositions inward.

Consider, for example, the system methanol−2-propanol−water; the residue curve map for this system, calculated using the NRTL parameters taken from the literature[20] and specified in Table 1, is shown in Figure 1a. A straight line distillation boundary connects the binary 2-propanol−water azeotrope with pure methanol and divides the composition space into two regions. According to rule 1, the column composition trajectories cannot cross this straight-line boundary, whichever side the feed is located. For either of the two feed locations, F_1 and F_2 in Figure 1a, boundary crossing is therefore forbidden.

For the system acetone−chloroform−methanol, we have three binary and one ternary azeotrope dividing the composition space into four regions by means of four distillation boundaries, which are all curved; see the residue curve map shown in Figure 1b, calculated using the NRTL parameters listed in Table 1. According to rule 2, the column trajectory obtained for operation with the feed located on the *concave* side of a boundary, with

Table 1. NRTL Parameters for Binary Mixtures at 101.3 kPa, Taken from Reference 20[a]

component *i*	component *j*	B_{ij}/K	B_{ji}/K	α_{ij}
water	ethanol	624.9174	−29.169	0.2937
water	acetone	602.6252	330.4768	0.5103
ethanol	acetone	188.8983	22.83319	0.3006
water	methanol	594.6299014	−182.60524	0.297
water	2-propanol	729.2208323	70.6618956	0.288
methanol	2-propanol	65.71121	−89.7427231	0.304
acetone	methanol	59.42076	149.0765	0.3003
acetone	chloroform	−327.6945	151.8924	0.3054
methanol	chloroform	−53.0728	671.975	0.2873

[a] These parameters are used along with $G_{ij} = \exp(-\alpha_{ij}\tau_{ij})$ and $\tau_{ij} = B_{ij}/T$.

* To whom correspondence should be addressed. Fax: +31 20 5255604. E-mail: krishna@science.uva.nl.

10.1021/ie010388m CCC: $22.00
Published on Web 02/26/2002

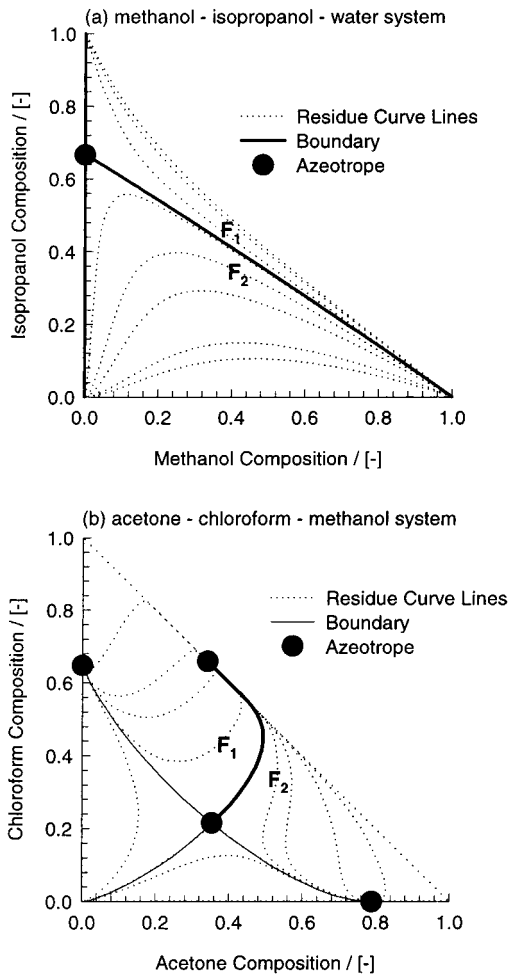

Figure 1. (a) Residue curve map for the methanol−2-propanol−water system, showing a straight-line distillation boundary and showing feed locations F_1 and F_2 on either side of the straight-line distillation boundary. (b) Residue curve map for the acetone−chloroform−methanol system showing feed locations F_1 and F_2 on the concave and convex sides of the highlighted distillation boundary.

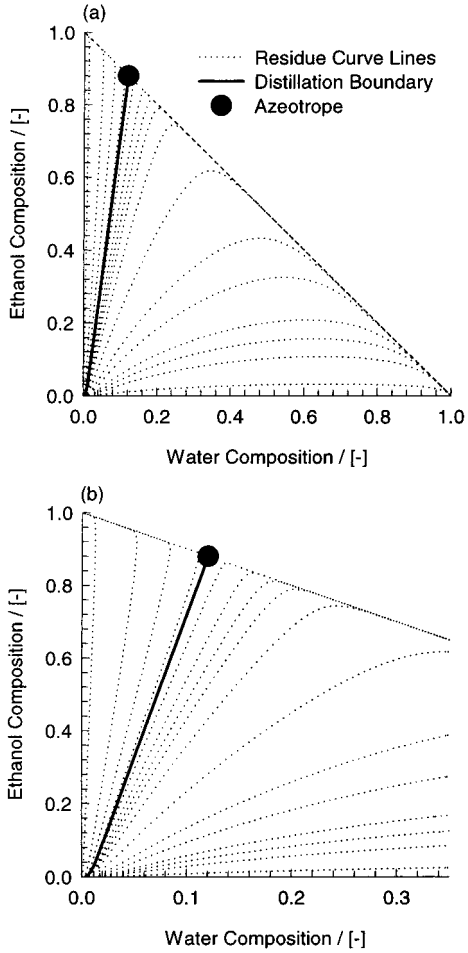

Figure 2. (a). Residue curve map for the water (1)−ethanol (2)−acetone (3) system, showing a straight-line distillation boundary and a binary minimum-boiling azeotrope between water and ethanol. (b) Zoomed-in version of part a.

say a composition as indicated by F_1, is able to cross that boundary. This has been demonstrated experimentally by Li et al.[4] Conversely, if the feed is located on the *convex* side, with say a composition as indicated by F_2, the boundary cannot be crossed.[12]

Most of the published literature simulation studies on the possibilities of crossing of distillation boundaries use the equilibrium (EQ) stage model. There is evidence in the published literature that experimentally measured composition profiles in distillation columns are better simulated with nonequilibrium (NEQ) stage models, in which proper account is taken of mass transfer in either fluid phase by use of the rigorous Maxwell−Stefan diffusion equations.[21−26] The Maxwell−Stefan formulation, based on the thermodynamics of irreversible processes, takes proper account of diffusional "coupling" between the species transfers; i.e., the flux of any species depends on the driving forces of all of the species present in the mixture. In a distillation column, the influence of species coupling manifests itself in significant differences in the component mass-transfer efficiencies. Castillo and Towler[27] computed nonequilibrium distillation lines for a sieve tray column and demonstrated that modest differences between the efficiencies of different components, caused by mass-transfer effects, could lead to significant differences in curvature between EQ and NEQ distillation column trajectories. They went on to show that, in some cases, differences in curvature could be exploited by the engineer in order to obtain process designs that could not be contemplated if mass-transfer effects were ignored and to show that some designs based solely on EQ models can become infeasible when mass transfer is considered.

Our major objective in this paper is to demonstrate that differences in the component efficiencies in ternary azeotropic distillation can cause column trajectories to cross even straight-line boundaries. To verify the boundary crossing phenomena, we performed experiments with the system water−ethanol−acetone. The residue curve map for this system, calculated with NRTL parameters listed in Table 1, is shown in Figure 2. This system shows a binary minimum-boiling azeotrope between water and ethanol; an almost-straight distillation boundary connects the azeotrope with pure acetone.

Experimental Section

Experimental Setup. The experiments were carried out in a laboratory-scale distillation column supplied by Schott Nederland B.V.; see Figure 3. The double-layered glass column with a vacuum between the inner and

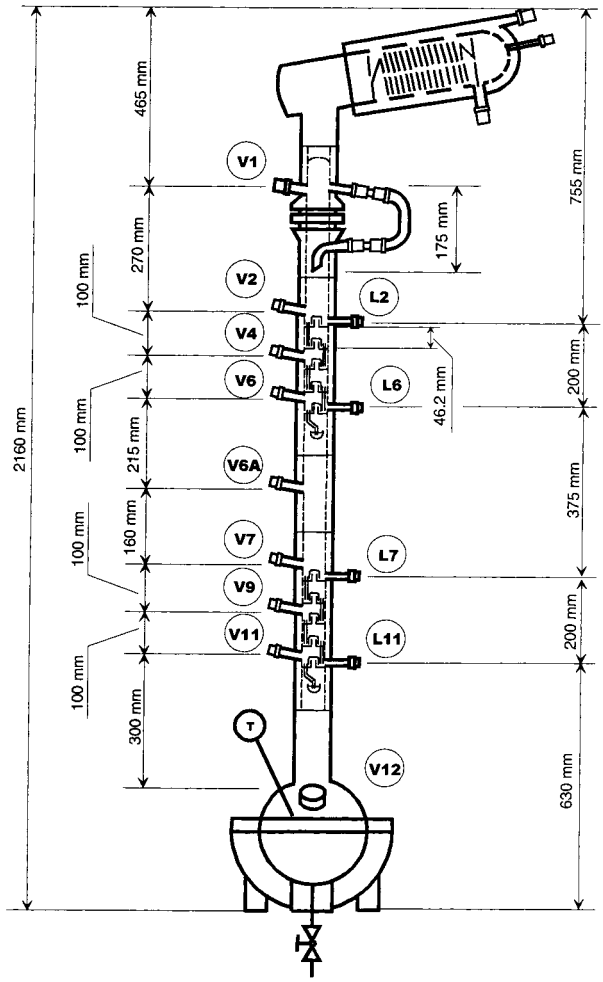

Figure 3. Schematic of a laboratory-scale distillation column, which includes a total condenser (1), a partial reboiler (12), 10 bubble-cap trays (2−11), and 13 draw-off faucets, 9 for vapor samples (V) and 4 for liquid samples (L).

Table 2. Bubble-Cap Tray Design of the Laboratory-Scale Distillation Column

column diameter	0.0500 m	hole pitch	0.0142 m
tray spacing	0.0462 m	cap diameter	0.0281 m
no. of flow passes	1	skirt clearance	0.0030 m
liquid flow path length	0.0308 m	slot height	0.0050 m
downcomer clearance	0.0039 m	active area (of the total area)	97.30%
deck thickness	0.0030 m	total hole area (of the total area)	8.27%
hole diameter	0.0142 m	downcomer area (of the total area)	1.35%
Weir type	circular	slot area	0.000221 m^2
Weir length	0.0182 m	riser area	0.000158 m^2
Weir height	0.0092 m	annular area	0.000462 m^2
Weir diameter	0.0058 m		

outer shells contains a total condenser (stage 1), a partial reboiler (stage 12), and 10 equal bubble-cap trays (stages 2−11) for which the dimensions are tabulated in Table 2 and pictured in Figure 4. The distillation column is divided into two sets of five bubble-cap trays by an intersection at which a continuous feed can be introduced to the column. Product streams can be tapped automatically from the condenser and manually from the reboiler. The glass distillation column has

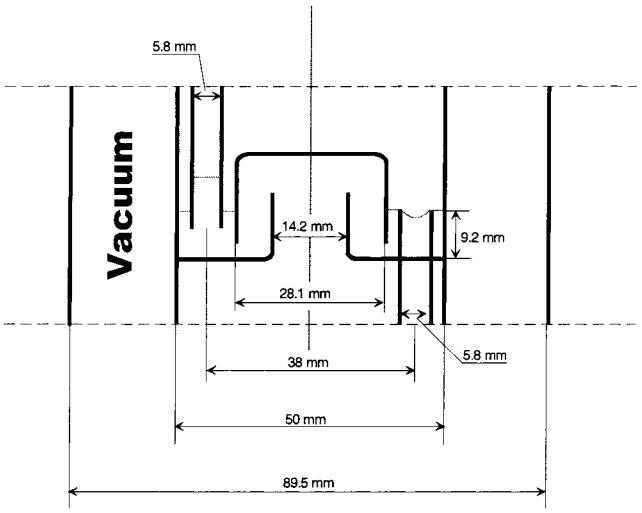

Figure 4. Details of the bubble cap.

several small openings of 10 mm in diameter, which are sealed with Teflon-coated septums. These openings enable liquid and vapor samples to be withdrawn by means of a syringe. The column has a total height of 2160 mm and a 50 mm inner diameter.

The reboiler is placed in a heating mantle, which is connected with a PC provided with the required software (Honeywell WinNT workstation 4.0; FIX MMI V 6.15/75-I/O-points runtime; OPTO CONTROL rel.2.2a). By means of the PC, the reboiler temperature as well as the feed and product flows can be controlled. Furthermore, it provides an automatic safety shutdown in case the column reboiler accidentally tends to dry up. The condenser is connected with a water tap, which supplies cooling water to the glass cooling tubes inside the condenser.

Experiments under total reflux conditions and atmospheric pressure were carried out with the system water−ethanol−acetone. For any given experiment, eight vapor and four liquid samples were taken from several stages (see Figure 3), and the temperature profile was measured with PT 100 sensors. Each sample volume was intentionally kept small (100 μL) to prevent changes in the composition profile during the entire experiment. The samples were first dissolved into a a reference solvent consisting of 1 vol % cyclohexane in 99 vol % *n*-propanol before injection into the gas chromatograph (GC; type GC8000 top with pressure/flow control) by means of an autosampler (type AS800). The channel inside the GC is made of stainless steel and has a total length of 1 m and a 0.125 inch inner diameter. The carrier gas used was helium because of its high thermal conductivity and chemical inertness. By analysis of samples of pre-prepared known compositions, the GC was carefully calibrated. More detailed descriptions of the experimental setup, measurement technique, GC analysis, and composition determination, including pictures of the column and bubble-cap trays, are available on our website: http://ct-cr4.chem.uva.nl/distillation/.

Experimental Results. The experimentally determined composition trajectories for a set of nine experiments are shown in Figure 5, along with the residue curve map. At total reflux the composition of the vapor leaving any given stage equals the composition of the liquid arriving at that stage from above. Therefore, the eight vapor and four liquid composition samples can be

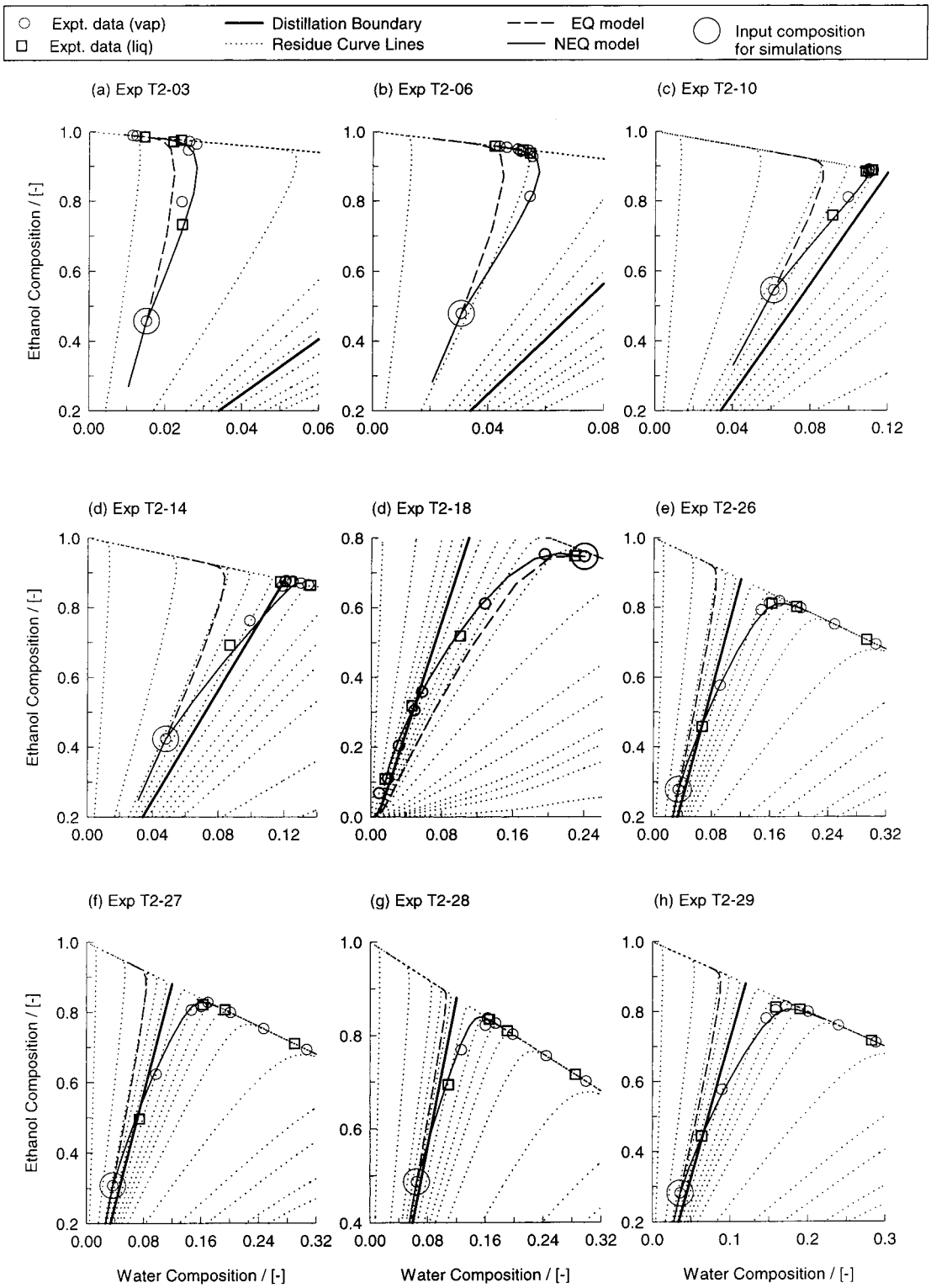

Figure 5. Experimental results (open circles for vapor samples and open squares for liquid samples) showing the column composition trajectories for the water (1)−ethanol (2)−acetone (3) system. Also shown are the simulation results showing the trajectories calculated by the EQ stage model and the NEQ stage model, along with the residue curve map. The large open circles represent the experimental composition specified in the simulations. In the NEQ model simulations, a bubble size of $d_b = 4.5$ mm was chosen.

combined when plotting the composition trajectories. In Figure 5, the vapor samples are denoted by open circles and the liquid samples by open squares. In experiments T2-03, T2-06, and T2-10, the column trajectories were all located on the left side of the distillation boundary (indicated by a thick line). All of the remaining six experiments clearly exhibit boundary-crossing phenomena. We also note that the experimental data points cut across the residue curves to the right at a sharp angle. In all of the experiments, except T2-18, there was no acetone present in the reboiler liquid. In the experiment T2-18, the acetone content in the initial charge to the system was high, and this resulted in a finite acetone content in the reboiler.

Clearly, the boundary-crossing phenomena are not in conformity with the assumption of thermodynamic

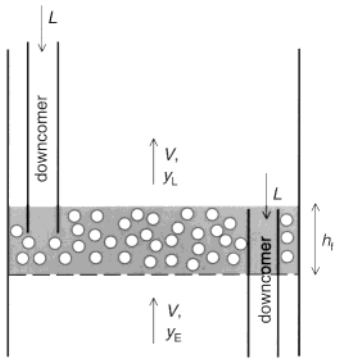

Figure 6. Schematic of the bubble froth regime on the tray.

phase equilibrium, which underlies the residue curve maps; this is evidenced by the fact that the experimental trajectories do not follow the residue curve map. To understand, and rationalize, the boundary-crossing phenomena, we develop a rigorous NEQ stage model.

NEQ Stage Model Development

The development of the NEQ stage model follows the ideas and concepts developed earlier by Taylor, Krishna, and others and described in earlier publications.[21−26] A brief review of the model development is given below. Consider first a single stage pictured in Figure 6. All of our experiments were carried out in the bubbly froth regime. Visual observations of tray operation (photographs are available at our website: http://ct-cr4.chem.uva.nl/distillation) showed that the bubbles were roughly of uniform size and shape. The steady-state component molar balance for a three-component distillation in tray columns is given by the two-dimensional matrix relation

$$V_b \frac{d(y)}{dh} = [K_{Oy}](y^* - y)a' \tag{1}$$

where a' is the interfacial area per unit volume of the dispersed bubble phase and V_b is the bubble rise velocity. Equation 1 can be rewritten in terms of the overall number of transfer units for the vapor phase $[NTU_{Oy}]$:

$$\frac{dy}{d\xi} = [NTU_{Oy}](y^* - y) \tag{2}$$

where $\xi = h/h_f$ is the dimensional distance along the froth and $[NTU_{Oy}]$ is defined as

$$[NTU_{Oy}] \equiv \int_0^{h_f} [[K_{Oy}]a'/V_b]\, dh \tag{3}$$

Carrying out the integration, assuming that the matrix of overall mass-transfer coefficients $[K_{Oy}]$ does not vary along the froth height, we obtain

$$[NTU_{Oy}] \equiv [K_{Oy}]a'h_f/V_b \equiv [K_{Oy}]a'\tau_V \tag{4}$$

From eq 4, we see that $[NTU_{Oy}]$ can be calculated from knowledge of $[K_{Oy}]$, the interfacial area per unit volume of vapor a', and the vapor-phase residence time τ_V. In our model we assume all of the bubbles to be spherical in shape with a diameter d_b. The interfacial area per unit volume of vapor a' is, therefore, given by

$$a' = 6/d_b \tag{5}$$

The vapor residence time is determined by

$$\tau_V = h_f/V_b \tag{6}$$

where h_f is the height of dispersion (froth); this is taken to be the height of the downcomer tube above the tray floor, i.e., 9.2 mm as seen in Figure 4. The bubble rise velocity V_b is estimated using the Mendelson equation,[28] recommended by Krishna et al.:[29]

$$V_b = \sqrt{\frac{2\sigma}{\rho_L d_b} + \frac{g d_b}{2}} \tag{7}$$

The overall matrix of mass-transfer coefficients $[K_{Oy}]$ is given by the addition of a resistance formula:

$$[K_{Oy}]^{-1} = [k_y]^{-1} + \frac{c_t^V}{c_t^L}[K_{eq}][k_x]^{-1} \tag{8}$$

in which $[K_{eq}]$ represents the diagonal matrix of K values and $[k_y]$ and $[k_x]$ are the partial transfer coefficient matrices for the vapor and liquid phases, respectively.

Let us consider the matrix of the multicomponent vapor mass-transfer coefficient $[k_y]$. The four elements $k_{y,ij}$ can be estimated from the mass-transfer coefficients of the constituent binary pairs, $\kappa_{y,ij}$, from

$$\begin{aligned} k_{y,11} &= \kappa_{y,13}(y_1\kappa_{y,23} + (1 - y_1)\kappa_{y,12})/S \\ k_{y,12} &= y_1\kappa_{y,23}(\kappa_{y,13} - \kappa_{y,12})/S \\ k_{y,21} &= y_2\kappa_{y,13}(\kappa_{y,23} - \kappa_{y,12})/S \\ k_{y,22} &= \kappa_{y,23}(y_2\kappa_{y,13} + (1 - y_2)\kappa_{y,12})/S \end{aligned} \tag{9}$$

where

$$S = y_1\kappa_{y,23} + y_2\kappa_{y,13} + y_3\kappa_{y,12} \tag{10}$$

For each of the binary pairs in the mixture, $\kappa_{y,ij}$ can be estimated from the following equation for instationary diffusion within a spherical bubble:[23]

$$Sh_{ij} \equiv \frac{\kappa_{y,ij} d_b}{D_{y,ij}} = \frac{2}{3}\pi^2 \left(\frac{\sum_{m=1}^{\infty} \exp\{-m^2\pi^2 Fo_{ij}\}}{\sum_{m=1}^{\infty} \frac{1}{m^2} \exp\{-m^2\pi^2 Fo_{ij}\}} \right); \quad ij = 12, 13, 23 \tag{11}$$

For Fourier numbers $Fo_{ij} \equiv 4D_{y,ij}\tau_V/d_b^2$ larger than 0.08, the Sherwood number reduces to the asymptotic value:

$$Sh_{ij} = 2\pi^2/3 \approx 6.58; \quad ij = 12, 13, 23 \tag{12}$$

For this steady-state limit, the binary vapor mass-transfer coefficients are given by

$$\kappa_{y,ij} = \frac{2\pi^2}{3}\frac{D_{y,ij}}{d_b} \tag{13}$$

Equation 13 leads to the important conclusion that $\kappa_{y,ij}$ would have a unity-power dependence on the vapor

diffusivity $D_{y,ij}$, which is in sharp contrast with the square-root dependence for small values of *Fo*, small vapor-phase residence times.

The matrix of the multicomponent liquid mass-transfer coefficient $[k_x]$ can be obtained analogously to eqs 9 and 10. The binary liquid mass-transfer coefficient $\kappa_{x,ij}$ can be obtained from the penetration model:

$$\kappa_{x.ij} = 2\sqrt{D_{x,ij}/\pi t_c} \tag{14}$$

where the contact time of the liquid with gas bubbles, t_c, is given by

$$t_c = d_b/V_b \tag{15}$$

In the above set of model equations, the only unknown parameter is the bubble diameter d_b. Once the bubble diameter is set, the system of equations can be solved. Substituting eq 8 into eq 4 gives us $[NTU_{Oy}]$. Assuming that $[NTU_{Oy}]$ on a single stage is constant, eq 2 can be integrated using the boundary conditions

$$\xi = 0 \text{ (inlet to tray) } (y) = y_E$$
$$\xi = 1 \text{ (outlet of tray) } (y) = y_L \tag{16}$$

to obtain the compositions leaving the distillation stage (detailed derivations are available in ref 23):

$$y^* - y_L = \exp[-[NTU_{Oy}]](y^* - y_E) \tag{17}$$

Introducing the matrix $[Q] \equiv \exp[-[NTU_{Oy}]]$, we may rewrite eq 17 in the form

$$y_L - y_E = [[I] - [Q]](y^* - y_E) \tag{18}$$

where $[I]$ is the identity matrix. The limiting case of the EQ stage model is obtained when the mass-transfer coefficients in either fluid phase attain large values; $[Q]$ reduces in this case to the null matrix, and the compositions leaving the tray (y_L) are equal to y^*, in equilibrium with the liquid leaving the tray.

The above set of equations model a single NEQ stage. More exhaustive details of this model including sample calculations for binary and ternary mixtures are available in Chapter 12 of Taylor and Krishna.[23] These equations are then incorporated into a rigorous stage-to-stage model incorporating the molar and energy balances as described in Chapter 14 of Taylor and Krishna.[23]

Simulation Strategy

Simulations of the total reflux experimental runs were carried out using both the EQ stage model and the rigorous NEQ stage model developed above. The operating pressure for all experiments was 101.3 kPa, and the ideal gas law was used. Activity coefficients were calculated using the NRTL interaction parameters, specified in Table 1, and the vapor pressures were calculated using the Antoine equations. The vapor phase was assumed to be thermodynamically ideal. The column consists of 12 stages, including the total condenser (stage 1) and partial reboiler (stage 12). The reflux flow rate (0.006 mol/s) and the bottom flow rate (0.0 mol/s) were used for specifying the column operations.

Because the column is operated at total reflux, the reflux flow rate determined the inner flow rates of vapor and liquid phases on each stage. Simulation of total reflux operations is "complicated" by the fact that there is no feed to the column at steady state. To overcome this problem, we specify one of the experimentally determined compositions of the streams leaving or entering a stage as an input parameter. The simulated composition profile of the total reflux run is forced to pass through this specified composition. In all of the experiments, except T2-18, we specified the vapor composition leaving stage 2 and entering the condenser in performing the simulations. This "input" composition is indicated by the large open circle in Figure 5. For experiment T2-18, where we have a finite acetone content in the reboiler, we used the experimentally determined composition of the vapor leaving the reboiler as an "input" composition for simulation purposes. The entire set of equations system was solved numerically by using Newton's method.[24,25] The NEQ implementation is available in the software program ChemSep, developed by Taylor.[23−26] Detailed information on ChemSep is available at http://www.chemsep.org and in the recent book by Kooijman and Taylor;[30] this book contains details of all thermodynamics and mass-transfer models for tray columns that have been implemented into the software.

Comparison of EQ and NEQ Simulations with Experiments

All experiments were simulated with the EQ stage model and the rigorous NEQ stage model. Let us consider one of the experiments (T2-26) in some detail. Figure 7a compares the EQ model with the experimental results. The large open circle represents the vapor composition leaving stage 2 and entering the condenser; this is specified in the simulations. We note that while the experimental points cross the distillation boundary, the EQ column trajectory does not and remains on the left side of the boundary. The EQ trajectory closely follows the residue curve map, shown in Figure 2. A further point to note is that while the experimental results show that in proceeding down the column (in the direction of the reboiler) the compositions get richer in water, the EQ simulations predict that these trays get progressively richer in ethanol. The NEQ model simulations require specification of the bubble diameter. For a range of bubble diameters of 3−5.5 mm, the NEQ trajectories have been plotted in Figure 7b. For $d_b = 3$ mm, the NEQ trajectory remains to the left of the distillation boundary and does not cross it. Decreasing the bubble diameter has the effect of increasing the mass-transfer coefficient (see eqs 13 and 14) and makes the NEQ model tend toward the EQ model. To match the EQ trajectory, the bubble size has to be 1.5 mm, or smaller. Conversely, increasing the bubble diameter decreases the mass-transfer coefficient and the NEQ trajectories move away from the EQ trajectory. For $d_b = 4.5$, 5, and 5 mm, all three NEQ trajectories cross the boundary. The best agreement with the experiments is obtained with $d_b = 4.5$ mm.

Let us consider the experimental run T2-18, for which the simulations were carried out by specifying the vapor compositions leaving the reboiler; see Figure 8. We see from Figure 8a that the EQ model does not cross the boundary and remains to the right side of it. Simulations for the NEQ model with varying bubble diameters are shown in Figure 8b. As in the case of T2-26, for $d_b = 3$ mm, the NEQ trajectory remains to the right of the distillation boundary and does not cross it. For $d_b = 4.5$,

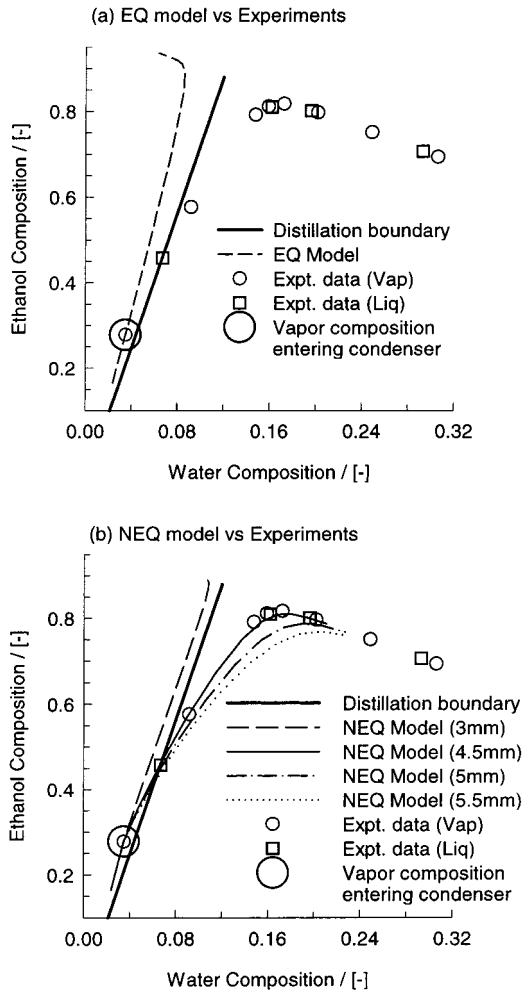

Figure 7. Simulation results compared with the experimental data (open circles for vapor samples and open squares for liquid samples) for run T2-26. (a) Here the EQ model is compared with the experimental results. (b) The NEQ model, for varying bubble diameters, is compared with the experimental results. The large open circle is the specified composition for the simulations; this corresponds to the vapor composition leaving stage 2 and entering the condenser.

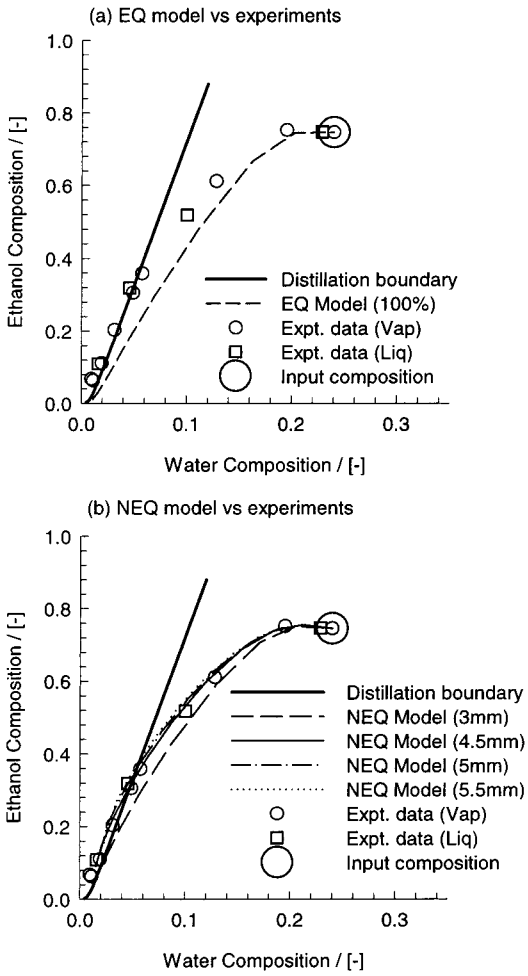

Figure 8. Simulation results compared with the experimental data (open circles for vapor samples and open squares for liquid samples) for run T2-18. (a) Here the EQ model is compared with the experimental results. (b) The NEQ model, for varying bubble diameters, is compared with the experimental results. The large open circle is the specified composition for the simulations; this corresponds to the vapor composition leaving the reboiler.

5, and 5 mm, all three NEQ trajectories cross the boundary. The best agreement with the experiments is again obtained with $d_b = 4.5$ mm.

The simulation results for the EQ and NEQ model, with $d_b = 4.5$ mm, for all of the experimental runs are shown in Figure 5, along with the experimental results.

Consider the runs T2-03, T2-06, and T2-10. For all of these runs, no boundary crossing is observed experimentally; see Figure 5a−c. Both EQ and NEQ models do not anticipate boundary crossing. The EQ model follows the trajectory dictated by the residue curve map, whereas the NEQ model has a tendency to cut across to the right of the residue curve. The predictions of the NEQ model are superior to that of the EQ model and in much better agreement with the experimentally measured composition trajectories. This tendency of the experiments to cut across to the right of the residue curves is strongly evident for run T2-10; here the NEQ model does a very good job of predicting the column trajectory.

Consider the runs T2-14, T2-18, T2-26, T2-27, T2-28, and T2-29 in Figure 5. For all of these runs, we experience boundary crossing and the NEQ model successfully anticipates this phenomenon. In all of the cases, the EQ model fails to cross the boundary and the EQ trajectory remains on one side of the boundary. For all of these runs, the experimental results show that in proceeding down the column (in the direction of the reboiler) the compositions get richer in water. The EQ simulations starting from the top tray (stage 2) predict that these trays get progressively richer in ethanol; this is qualitatively different from the experimental observations.

To show that the choice of the bubble diameter $d_b = 4.5$ mm is not merely a "convenient fit" of our ternary experiments, we also carried a set of eight experiments with the binary mixture ethanol−water and sets of four experiments with the binary mixtures water−methanol, water−2-propanol, and methanol−2-propanol in the same experimental setup. The column (vapor) composition trajectories are shown in Figure 9, along with the NEQ model predictions taking $d_b = 4.5$ and 5.0 mm. We note that the composition profiles are equally well predicted by taking the bubble diameter to be either 4.5 or 5 mm. The NEQ simulations were carried out by specifying the vapor composition leaving the reboiler (stage 12); as we proceed up the column, we approach the azeotropic composition. The NEQ simulations de-

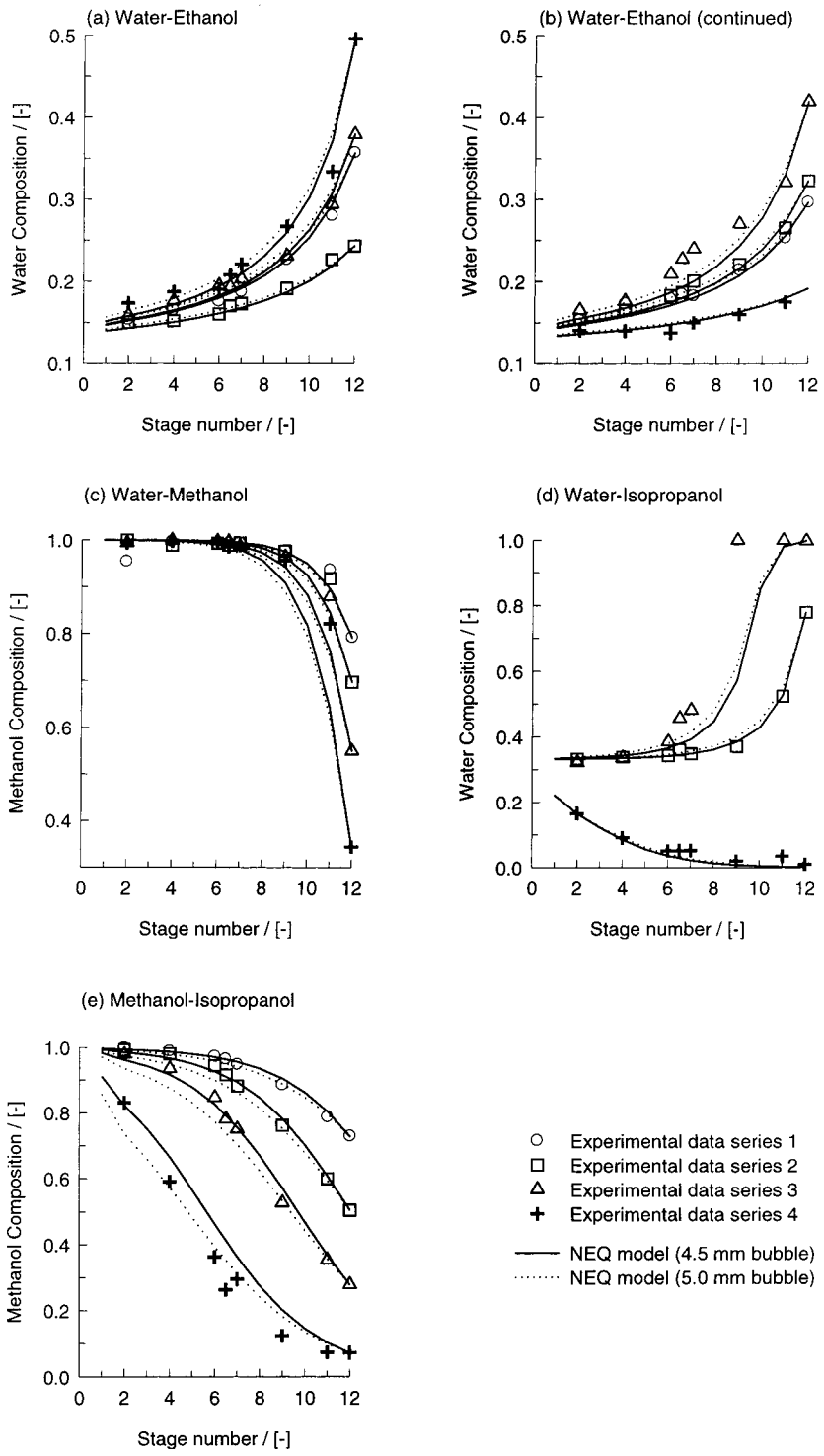

Figure 9. Experimental results (open circles for vapor samples) showing the column composition trajectories for the water (1)−ethanol (2), water (1)−methanol (2), water (1)−2-propanol (2), and methanol (1)−2-propanol (2) binary systems. Also shown are the simulation results showing the trajectories calculated by the NEQ stage model. For each binary, the experimental vapor composition leaving the reboiler is specified in the simulations. In the NEQ model simulations, bubble sizes of $d_b = 4.5$ mm (solid line) and 5.0 mm (dotted line) were chosen.

scribe the column trajectories very well for all of the experimental results and therefore support our NEQ simulations for the studied ternary system.

Component Murphree Efficiencies in Ternary Distillation

We may conclude from the foregoing that boundary crossing is caused by *multicomponent* mass-transfer effects. To explain this in some detail, we consider run T2-26. The values of the binary pair vapor diffusivities, $D_{y,12}$, $D_{y,13}$, and $D_{y,23}$, for water (1)−ethanol (2)−acetone (3) are specified in Table 3, along with the corresponding liquid-phase coefficients. The vapor-phase diffusivities of the three binary pairs are estimated using the Fuller−Schettler−Giddings equation; details of the estimation procedure are to be found in Kooijman and

Table 3. Physical and Transport Properties per Stage of Experiment T2-26 for the Water (1)−Ethanol (2)−Acetone (3) System Obtained by NEQ Model Simulations (Bubble Diameter = 4.5 mm)

stage no.	$D_{y,12}$ [10^{-6} m^2/s]	$D_{y,13}$ [10^{-6} m^2/s]	$D_{y,23}$ [10^{-6} m^2/s]	$D_{x,12}$ [10^{-9} m^2/s]	$D_{x,13}$ [10^{-9} m^2/s]	$D_{x,23}$ [10^{-9} m^2/s]	σ [10^{-2} N/m]	ρ_L [kg/m^3]	V_b [m/s]	τ_V [s]	Fo_{12}	Fo_{13}	Fo_{23}
2	19.9	17.3	8.58	7.42	7.83	4.44	2.58	761	0.193	0.0477	0.188	0.163	0.081
3	20.1	17.5	8.68	6.91	6.69	3.95	2.77	766	0.195	0.0471	0.187	0.163	0.081
4	20.4	17.7	8.81	6.42	5.63	3.5	3.01	770	0.199	0.0463	0.187	0.162	0.081
5	20.7	18	8.95	6.08	4.85	3.17	3.26	773	0.202	0.0456	0.186	0.162	0.081
6	21	18.2	9.07	5.95	4.42	3.01	3.46	773	0.205	0.0449	0.186	0.162	0.080
7	21.2	18.4	9.15	5.94	4.24	2.95	3.59	773	0.207	0.0445	0.186	0.162	0.080
8	21.3	18.5	9.2	5.94	4.16	2.94	3.69	773	0.208	0.0442	0.186	0.162	0.080
9	21.4	18.5	9.23	5.91	4.11	2.94	3.76	773	0.209	0.0440	0.186	0.161	0.080
10	21.4	18.6	9.24	5.86	4.07	2.93	3.83	774	0.210	0.0438	0.185	0.161	0.080
11	21.4	18.6	9.24	5.78	4.03	2.93	3.92	774	0.211	0.0436	0.184	0.160	0.080

Taylor.[30] The estimated values of the Fourier numbers calculated using

$$Fo_{ij} = 4D_{y,ij}\tau_V/d_b^2 \tag{19}$$

are also given in Table 3, along with the values of the surface tension (σ) and liquid density (ρ_L) that are needed in order to estimate the single bubble rise velocity (V_b) and thus the vapor residence time (τ_V) using eqs 6 and 7. From Table 3, we see that the *Fo* values exceed 0.08 in all cases, justifying the use of eq 13 for estimation of the vapor-phase mass-transfer coefficients $\kappa_{y,ij}$ of the binary pairs in the mixture; $\kappa_{y,ij}$ values have a unity-power dependence on the vapor diffusivities $D_{y,ij}$. By evaluation of the individual contributions of the liquid and vapor phases in eq 18, it can be verified that the mass-transfer resistance is predominantly in the vapor phase. The liquid-phase resistance contributes less than 10% of the total resistance; this conclusion was found to be valid for all of the nine experimental runs carried out in this study.

To understand the phenomena of boundary crossing, we consider the component Murphree stage efficiencies, defined by

$$E_i = \frac{y_{i,L} - y_{i,E}}{y_i^* - y_{i,E}}, \quad i = 1-3 \tag{20}$$

For the EQ model, the component efficiencies are all equal to unity. For the NEQ model, the component efficiencies will, in general, differ from one another. To illustrate this, we present the calculations of E_i for run T2-26 in Figure 10a obtained from NEQ simulations with a bubble diameter of 4.5 mm. It is clear that the component Murhpree efficiencies are all different from one another and vary from stage to stage. The origin of the differences in E_i can be traced to the differences in the binary pair vapor diffusivities, $D_{y,12}$, $D_{y,13}$, and $D_{y,23}$. We note that the coefficient $D_{y,23}$ is about half of the other coefficients. The difference between binary pair diffusivities causes the component efficiency values to be different from one another. The variation of the ethanol efficiency is particularly "strange" in that on stage 9 the value is close to zero whereas on stage 10 the component efficiency exceeds unity. The reason for the strange behavior of the ethanol efficiency is to be found in the driving force (denominator term in eq 20) which is shown in Figure 10b; the driving force changes sign between stages 9 and 10, and the magnitude of the driving force is, therefore, vanishingly small on stages 9 and 10. The transfer of ethanol on these trays is dictated by the transfer of the other two components because of coupling effects which are properly accounted for in the Maxwell−Stefan formulation.[21−23] For binary mixtures, component efficiencies are bounded and lie between zero and unity; for mixtures with three or more components, component efficiencies are unbounded and can assume values ranging from $-\infty$ to $+\infty$. If the binary $D_{y,ij}$ were close to one another, the differences in the component efficiencies would be negligible. Differences in the component efficiencies cause the actual composition trajectory followed on any given stage ($y_{i,L} - y_{i,E}$) to deviate from the trajectory dictated by the equilibrium vector ($y_i^* - y_{i,E}$).

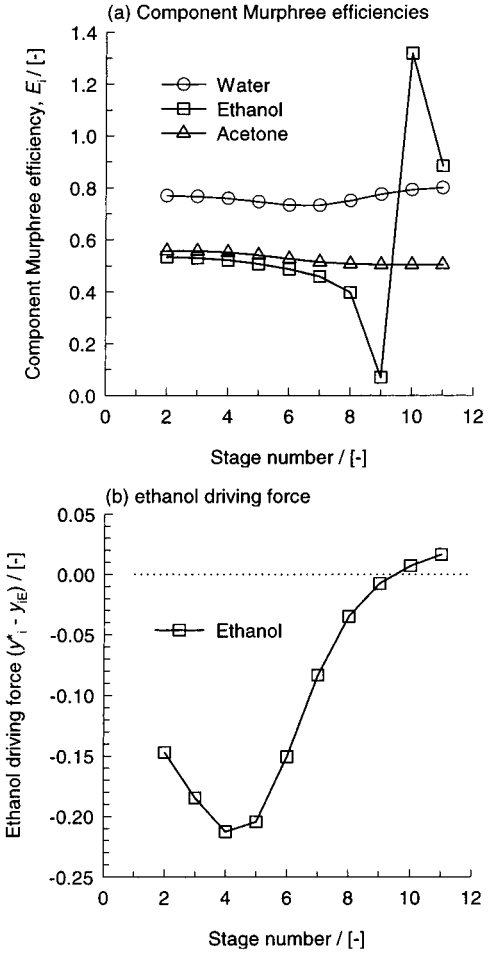

Figure 10. (a) Component efficiencies along the column for the experiment T2-26 and (b) the driving force for ethanol at each stage, calculated by the NEQ stage model. In the NEQ model simulations, a bubble size of d_b = 4.5 mm was chosen.

For various vapor compositions entering any given stage, we have plotted in Figure 11a the actual composition vector ($y_{i,L} - y_{i,E}$), calculated from the NEQ model

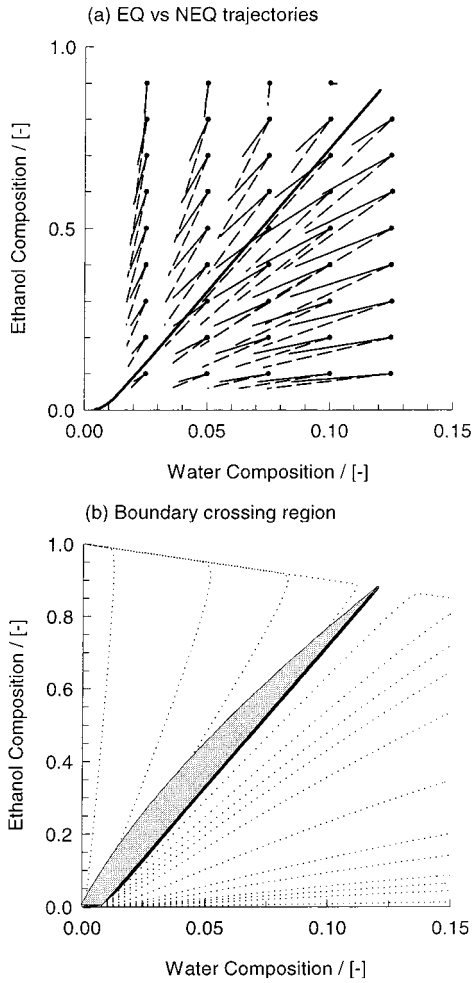

Figure 11. (a) Calculated direction vectors using the EQ stage model (100% efficiency for all components, denoted by dashed lines) and the NEQ stage model (denoted by continuous lines). In the NEQ model simulations, a bubble size of $d_b = 4.5$ mm was chosen. (b) All starting compositions (of vapor entering the condenser) within the gray-shaded region will cross the distillation boundary to the right of this boundary.

(taking a bubble diameter of 4.5 mm) along with the equilibrium vector ($y_i^* - y_{i,E}$). The angle between the NEQ trajectory (continuous line) and the EQ trajectory (dashed line) increases when the differences in the component efficiencies increase. If all of the component efficiencies were equal to one another, the NEQ and EQ trajectories would coincide. We see from Figure 11a that the NEQ trajectory has a tendency to cut across to the right of the EQ trajectory, precisely as has been observed in the experiments (cf. Figure 5). It is this tendency to cut toward the right of the composition space that causes boundary crossing. By performing several NEQ simulations with various starting compositions of the vapor entering the condenser, we can determine the region within which the column trajectories will cross the distillation boundary and end up with reboiler compositions in the right region. This boundary-crossing region is shown as the gray-shaded area in Figure 11b. It can be verified that the starting compositions for the three runs T2-03, T2-06, and T2-10 lie to the left of the gray-shaded region; no boundary crossing is, therefore, observed for these runs. For the remainder of the experiments, the starting vapor compositions entering the condenser lie within the shaded region; boundary crossing is observed for all of the six runs.

Conclusions

The following major conclusions can be drawn from the work presented in this paper.

1. The measured composition trajectories during distillation of water−ethanol−acetone under total reflux conditions in a bubble-cap distillation column clearly demonstrate that crossing of a straight-line distillation boundary is possible.

2. An NEQ stage model is able to model the experimental results. The experimental results agree very well with the developed model in which a bubble size of 4.5 mm is chosen. The NEQ model correctly anticipates boundary crossing.

3. An EQ stage model fails to anticipate boundary crossing in any experiment. The EQ model provides a much poorer representation of the column composition trajectories and does not even agree qualitatively with the experimental results. While the experimental trajectory shows that the column gets progressively richer in water as we proceed down to the reboiler, the EQ trajectory predicts that the column gets progressively richer in ethanol; see Figure 5.

4. Boundary crossing is anticipated by the NEQ model regardless of which end of the column the simulations are made to start from; this is evidenced by the NEQ trajectories for T2-26 (see Figure 7) and T2-18 (see Figure 8) for which the specified compositions correspond respectively to that of the vapor leaving the top tray and bottom reboiler.

5. The differences in the NEQ and EQ trajectories emanates from differences in the component Murphree efficiencies, which in turn can be traced to differences in the binary pair vapor-phase diffusivities $D_{y,ij}$.

The overall conclusion to be drawn from this work is that, for reliable design of the distillation of homogeneous azeotropic systems, we must adopt the NEQ stage model.

Acknowledgment

The authors acknowledge a grant from The Netherlands Organization for Scientific Research (NWO), Chemical Sciences Division (CW), for investigations on three-phase distillation. The authors are grateful to R. Taylor and H. Kooijman for providing the code to ChemSep, which was used in this study after appropriate modification to include the rigid bubble model.

Notation

a' = interfacial area per unit volume of vapor bubbles [m^2/m^3]
B_{ij} = NRTL parameters; see Table 1 [K]
c_t = mixture molar density [mol/m^3]
c_t^L = mixture molar density of the liquid phase [mol/m^3]
c_t^V = mixture molar density of the vapor phase [mol/m^3]
d_b = bubble diameter [m]
$D_{x,ij}$ = Maxwell−Stefan diffusivity for pair $i-j$ for the liquid phase [m^2/s]
$D_{y,ij}$ = Maxwell−Stefan diffusivity for pair $i-j$ for the vapor phase [m^2/s]
E_i = component Murphree efficiency
Fo = Fourier number, $Fo \equiv 4D_y\tau_V/d_b^2$
G_{ij} = NRTL parameters; see Table 1

g = acceleration due to gravity [m/s^2]
h = distance along the froth height [m]
h_f = height of dispersion [m]
k_{ij} = element for the matrix of the multicomponent mass-transfer coefficient [m/s]
$[k_x]$ = matrix of the multicomponent liquid mass-transfer coefficients [m/s]
$[k_y]$ = matrix of the multicomponent vapor mass-transfer coefficients [m/s]
$[K_{eq}]$ = diagonal matrix of K values
$[K_{Oy}]$ = matrix of the multicomponent overall mass-transfer coefficients [m/s]
$[NTU_{Oy}]$ = matrix of the overall number of vapor phase-transfer units
S = parameter defined in eq 10 [m/s]
Sh = Sherwood number
t_c = liquid-bubble contact time [s]
T = temperature [K]
V_b = single bubble rise velocity [m/s]
x_i = liquid composition for component i
y_i = vapor composition for component i

Greek Letters

α_{ij} = nonrandomness parameter in the NRTL equation, see Table 1
$\kappa_{x,ij}$ = binary Maxwell−Stefan liquid mass-transfer coefficients [m/s]
$\kappa_{y,ij}$ = binary Maxwell−Stefan vapor mass-transfer coefficients [m/s]
ρ_L = density of the liquid [kg/m^3]
μ_L = liquid viscosity [Pa s]
σ = surface tension [N/m]
τ_V = vapor-phase residence time [s]
τ_{ij} = NRTL parameters; see Table 1
ξ = dimensionless distance along the dispersion or column height

Subscripts

b = bubble
f = froth
i = component i
j = component j
Oy = overall parameter referring to the vapor phase
ref = reference
t = total mixture
x = x phase (liquid)
y = y phase (vapor)

Superscripts

L = liquid phase
V = vapor phase
* = equilibrium state

Literature Cited

(1) Stichlmair, J. G.; Fair, J. R. *Distillation principles and practice*; Wiley-VCH: New York, 1998.

(2) Doherty, M. F.; Malone, M. F. *Conceptual design of distillation systems*; McGraw-Hill: New York, 2001.

(3) Widagdo, S.; Seider, W. D. Azeotropic distillation. *AIChE J.* **1996**, *42*, 96−130.

(4) Li, Y.; Chen, H.; Liu, J. Composition profile of an azeotropic continuous distillation with feed composition on a ridge or in a valley. *Ind. Eng. Chem. Res.* **1999**, *38*, 2482−2484.

(5) Knapp, J. P.; Doherty, M. F. A new pressure-swing-distillation process for separating homogeneous azeotropic mixtures. *Ind. Eng. Chem. Res.* **1992**, *31*, 346−357.

(6) Foucher, E. R.; Doherty, M. F.; Malone, M. F. Automatic screening of entrainers for homogeneous azeotropic distillation. *Ind. Eng. Chem. Res.* **1991**, *30*, 760−772.

(7) Knapp, J. P.; Doherty, M. F. Thermal integration of homogeneous azeotropic distillation sequences. *AIChE J.* **1990**, *36*, 969−984.

(8) Pham, H. N.; Doherty, M. F. Design and synthesis of azeotropic distillation. 2. Residue curve maps. *Chem. Eng. Sci.* **1990**, *45*, 1837−1843.

(9) Julka, V.; Doherty, M. F. Geometric behavior and minimum flows for nonideal multicomponent distillation. *Chem. Eng. Sci.* **1990**, *45*, 1801−1822.

(10) Barbosa, D.; Doherty, M. F. The simple distillation of homogeneous reactive mixtures. *Chem. Eng. Sci.* **1988**, *43*, 541−550.

(11) Fidkowski, Z. T.; Doherty, M. F.; Malone, M. F. Feasibility of separations for distillation of nonideal ternary mixtures. *AIChE J.* **1993**, *39*, 1303−1321.

(12) Levy, S. G.; van Dongen, D. B.; Doherty, M. F. Design and synthesis of homogeneous azeotropic distillation. 2. Minimum reflux calculations for nonideal and azeotropic columns. *Ind. Eng. Chem. Fundam.* **1985**, *24*, 463−474.

(13) Wahnschafft, O. M.; Koehler, J. W.; Westerberg, A. W. Homogeneous azeotropic distillation—Analysis of separation feasibility and consequences for entrainer selection and column design. *Comput. Chem. Eng.* **1994**, *18*, S31−S35.

(14) Wahnschafft, O. M.; Koehler, J. W.; Blass, E.; Westerberg, A. W. The product composition regions of single-feed azeotropic distillation-columns. *Ind. Eng. Chem. Res.* **1992**, *31*, 2345−2362.

(15) Doherty, M. F.; Caldarola, G. A. Design and synthesis of homogeneous azeotropic distillations. 3. The sequencing of columns for azeotropic and extractive distillation. *Ind. Eng. Chem. Fundam.* **1985**, *24*, 474−485.

(16) Van Dongen, D. B.; Doherty, M. F. Design and synthesis of homogeneous azeotropic distillations. 1. Problem formulation for a single column. *Ind. Eng. Chem. Fundam.* **1985**, *24*, 454−463.

(17) Pelkonen, S.; Kaesemann, R.; Gorak, A. Distillation lines for multicomponent separation in packed columns: theory and comparison with experiment. *Ind. Eng. Chem. Res.* **1997**, *36*, 5392−5398.

(18) Castillo, F. J. L.; Thong, D. Y. C.; Towler, G. P. Homogeneous azeotropic distillation. 2. Design procedure for sequences of columns. *Ind. Eng. Chem. Res.* **1998**, *37*, 998−1008.

(19) Rev, E. Crossing of valleys, ridges and simple distillation boundaries by distillation in homogeneous ternary mixtures. *Ind. Eng. Chem. Res.* **1992**, *31*, 893−901.

(20) Gmehling, J. L.; Onken, U. *Vapor−liquid equilibrium data collection*; Dechema: Frankfurt, Germany, 1977.

(21) Krishna, R.; Wesselingh, J. A. The Maxwell−Stefan approach to mass transfer. *Chem. Eng. Sci.* **1997**, *52*, 861−911.

(22) Wesselingh, J. A.; Krishna, R. *Mass transfer in multicomponent mixtures*; Delft University Press: Delft, The Netherlands, 2000.

(23) Taylor, R.; Krishna, R. *Multicomponent mass transfer*; John Wiley: New York, 1993.

(24) Krishnamurthy, R.; Taylor, R. Nonequilibrium stage model of multicomponent separation processes. *AIChE J.* **1985**, *32*, 449−465.

(25) Taylor, R.; Kooijman, H. A.; Hung, J. S. A second generation nonequilibrium model for computer-simulation of multicomponent separation processes. *Comput. Chem. Eng.* **1994**, *18*, 205−217.

(26) Baur, R.; Taylor, R.; Krishna, R.; Copati, J. A. Influence of mass transfer in distillation of mixtures with a distillation boundary. *Chem. Eng. Res. Des.* **1999**, *77*, 561−565.

(27) Castillo, F. J. L.; Towler, G. P. Influence of multicomponent mass transfer on homogeneous azeotropic distillation. *Chem. Eng. Sci.* **1998**, *53*, 963−976.

(28) Mendelson, H. D. The prediction of bubble terminal velocities from wave theory. *AIChE J.* **1967**, *13*, 250−253.

(29) Krishna, R.; Urseanu, M. I.; van Baten, J. M.; Ellenberger, J. Wall effects on the rise of single gas bubbles in liquids. *Int. Commun. Heat Mass Transfer* **1999**, *26*, 781−790.

(30) Kooijman, H. A.; Taylor, R. *The ChemSep book*; Libri Books: Books on Demand, Norderstedt, Germany, 2001. See also the website: www.chemsep.org.

Received for review May 1, 2001
Revised manuscript received January 4, 2002
Accepted January 8, 2002

IE010388M